Long-Term Statistics of Riming in Nonconvective Clouds Derived from Ground-Based Doppler Cloud Radar Observations

STEFAN KNEIFEL

Institute for Geophysics and Meteorology, University of Cologne, Cologne, Germany

DMITRI MOISSEEV

Institute for Atmospheric and Earth System Research/Physics, Faculty of Science, University of Helsinki, and Finnish Meteorological Institute, Helsinki, Finland

(Manuscript received 7 January 2020, in final form 27 July 2020)

ABSTRACT: Riming is an efficient process of converting liquid cloud water into ice and plays an important role in the formation of precipitation in cold clouds. Due to the rapid increase in ice particle mass, riming enhances the particle's terminal velocity, which can be detected by ground-based vertically pointing cloud radars if the effect of vertical air motions can be sufficiently mitigated. In our study, we first revisit a previously published approach to relate the radar mean Doppler velocity (MDV) to rime mass fraction (FR) using a large ground-based in situ dataset. This relation is then applied to multiyear datasets of cloud radar observations collected at four European sites covering polluted central European, clean maritime, and Arctic climatic conditions. We find that riming occurs in 1%–8% of the nonconvective ice containing clouds with median FR between 0.5 and 0.6. Both the frequency of riming and FR reveal relatively small variations for different seasons. In contrast to previous studies, which suggested enhanced riming for clean environments, our statistics indicate the opposite; however, the differences between the locations are overall small. We find a very strong relation between the frequency of riming and temperature. While riming is rare at temperatures lower than −12°C, it strongly increases toward 0°C. Previous studies found a very similar temperature dependence for the amount and droplet size of supercooled liquid water, which might be closely connected to the riming signature found in this study. In contrast to riming frequency, we find almost no temperature dependence for FR.

KEYWORDS: Climatology; Cloud microphysics; Cloud water/phase; Ice particles; Icing; Cloud retrieval

1. Introduction

Riming denotes the collision and accretion of supercooled liquid water (SLW) drops onto ice particles in clouds. Besides depositional growth and aggregation, riming is one of the key precipitation formation processes. Riming is a fast and efficient process that enhances the mass of ice particles by converting SLW directly into ice. One central effect of riming is the enhancement of ice particle terminal velocity due an increasing particle density. Theoretical as well as observational studies showed that while the total particle mass increases due to the added frozen drops, the cross-sectional area remains relatively constant (Heymsfield 1982; Morrison and Grabowski 2008; Jensen and Harrington 2015; Erfani and Mitchell 2017; Seifert et al. 2019). The particle size begins to increase due to riming once the ice structure becomes sufficiently filled in with rimed ice. This increase in mass and fall speed leads to an overall increased precipitation flux (Colle et al. 2014; Grazioli et al. 2015). Depending on the climatic region, riming can contribute substantially to the total snowfall mass on the ground. Typical values for this contribution have been found to be 30%–40% in the Sierra Nevada (Mitchell et al. 1990), 5%–40% in southern Finland (Moisseev et al. 2017), and more than 50% in Japan (Harimaya and Sato 1989).

Riming also plays a key role for secondary ice processes such as rime splintering (Hallett and Mossop 1974) or ice–ice collisions (Field et al. 2017). A strong relation between the efficiency of riming and the size of the supercooled droplets has been found in several observational studies (Borys et al. 2003; Lowenthal et al. 2011). The drop size must be larger than 10 μm for the supercooled drops to efficiently collide and freeze onto the ice particles (Wang and Ji 2000). On one hand, this relation implies a possible link between global aerosol concentrations and precipitation (Lohmann 2004). For the same amount of liquid water, a higher aerosol concentration would cause the average droplet size to decrease thus lowering their efficiency to rime. On the other hand, due to the link between droplet size and riming, any observational technique which is able to detect riming, might also be useful for detection of aircraft icing conditions. Unfortunately, no observational statistics of the presence and intensity of riming in different climatic regions are currently available.

During recent years, modeling of riming has made significant progress. New developments range from detailed process simulations (Leinonen and Szyrmer 2015; Seifert et al. 2019) to explicit modeling the evolution of ice habit due to riming (Jensen and Harrington 2015) and new approaches for bulk models to represent the continuous nature of riming rather than the common artificial sorting of ice in predefined classes (Morrison and Milbrandt 2015). Also

Denotes content that is immediately available upon publication as open access.

Corresponding author: Stefan Kneifel, skneifel@meteo.uni-koeln.de

DOI: 10.1175/JAS-D-20-0007.1

modern ground-based in situ sensors provide an automatic classification of the rimed particles (Garrett and Yuter 2014; Praz et al. 2017) and derivation of their rime mass fraction (Moisseev et al. 2017).

To better understand riming inside clouds, radar remote sensing techniques have been investigated with respect to their information content related to riming. Polarimetric radar approaches are mainly based on the changing particle shape and density due to riming (Kumjian et al. 2014, 2016; Li et al. 2018; Schrom and Kumjian 2018). Recent studies (Vogel and Fabry 2018; Li et al. 2018) show that the polarimetric signatures caused by riming are weaker than the variability of polarimetric variables between different cases. An explanation for the overall weak polarimetric signals due to riming might be that the shape of rimed ice and aggregates changes in a similar way during their growth. In addition, rimed particles can be assumed to be often mixed with other ice particles in the same radar volume (Kalesse et al. 2016), which can cause the polarimetric signature to be obscured. However, riming can be indirectly detected by polarimetric radars, for example when rimed particles are involved in secondary ice processes, such as rime splintering (Sinclair et al. 2016; Giangrande et al. 2016; Kumjian and Lombardo 2017). Combinations of multiple radar frequencies have recently been found to be sensitive to riming (Kneifel et al. 2015); however, their quantitative use is currently under investigation (Leinonen et al. 2018; Mason et al. 2018).

When pointing Doppler radars vertically, the presence of rimed particles can be detected by their increased terminal velocity. For unrimed snowflakes generated by aggregation, the effect of increasing mass at larger sizes on terminal velocity is mostly compensated by the additional drag caused by the larger cross-sectional area exposed to the airflow. In situ and radar observations clearly show that larger snowflakes fall with a terminal velocity (assuming surface pressure conditions) of around $1\ \mathrm{m\,s^{-1}}$ almost independent of size (Zawadzki et al. 2001). Larger fall velocities exceeding, for example, values of $1.5\ \mathrm{m\,s^{-1}}$ can be reliably assigned to riming as long as melting and vertical air motions can be excluded. The first approach of deriving a quantitative relation between riming and radar Doppler velocity was presented by Mosimann (1995). Based on in situ samples of ice particles collected on a mountain slope and observations with a vertically pointing X-band radar operated in the valley, Mosimann (1995) derived a relation of an empirically defined scale of the degree of riming and the measured Doppler velocity. Using observational relations between the degree of riming and rime mass fraction for different ice particle habits (Mosimann et al. 1994), the Doppler velocity can be linked to the rime mass fraction of the particles (Lin et al. 2011). The method is, however, limited to nonconvective clouds as an implicit assumption of this techniques is that the measured Doppler velocity is identical to the terminal fall velocity of the particles. While random air motions due to turbulence and gravity waves can be successfully removed by temporal averaging, more temporally persistent up- and downdrafts as caused, for example, by convective systems or orographic flow cannot be reliably corrected for.

In this study, we first revisit Mosimann's pioneering approach to link Doppler velocities and riming in section 2. For this, we utilize long-term in situ observations of ice and snow particles at the ground collected at a site in Finland (Moisseev et al. 2017; von Lerber et al. 2017). Based on the derived ice and snow particle properties, their associated mean radar Doppler velocity are simulated which allows us to relate them to measured rime mass fractions (defined as ratio between rime mass and total particle mass). Our new relations are thus based on a more robust basis of observed snowfall events but also provide relations for widely used cloud radar frequencies [X, Ka, and W bands while only X band is provided in Mosimann (1995)]. We apply the new relations to multiyear radar observations processed with the CloudNet algorithm (Illingworth et al. 2007) from four European sites including one site located in the Arctic. Statistics of the derived riming frequency and rime mass fraction are analyzed in section 3 with respect to their seasonal dependence and relation to in-cloud temperature. A discussion of the results and a summary of the main findings is given in section 4.

2. Data and methods

a. Revisited mean Doppler velocity–riming relation

There are several approaches that are used to quantify riming of ice particles. Following (Mosimann et al. 1994), the degree of riming is often used to describe the impact of accreted water droplets on the visual appearance of ice particles (Garrett and Yuter 2014; Praz et al. 2017). In numerical weather prediction models, the rime mass fraction, which defines the fraction of total particle mass gained by riming is preferred (Morrison and Milbrandt 2015). Moisseev et al. (2017) have used the observations of particle size distribution and mass as derived from ground-based precipitation video imager observations (von Lerber et al. 2017) to derive a proxy for the rime mass fraction. Assuming that the relation of mass m and maximum particle size $D_{\max}$ follows a power law and its exponent β is constant, the rime mass fraction (FR) is related to the prefactor α as (Moisseev et al. 2017; Li et al. 2018):

$$m = \alpha D_{\max}^{\beta} = \frac{\alpha_{\mathrm{us}}}{1 - \mathrm{FR}} D_{\max}^{\beta}, \tag{1}$$

where $m_{\mathrm{us}} = \alpha_{\mathrm{us}} D_{\max}^{\beta}$ is the reference mass–dimensional relation for unrimed snowflakes. This relation can either be selected from literature (Mason et al. 2018), for example, by using the relation by Brown and Francis (1995), or using a statistical approach (Moisseev et al. 2017). Assuming that observed particles with the lowest 5% density values are unrimed, Moisseev et al. (2017) have derived the following $m_{\mathrm{us}}(D_{\max})$ relation:

$$m_{\mathrm{us}} = 0.0053 D_{\max}^{2.05}. \tag{2}$$

Note that m_{us} is assumed to be in grams and $D_{\max}$ in centimeters. There are several ways how FR can be estimated from the in situ observations. Moisseev et al. (2017) matched measured and computed mean ensemble density of snowflakes, while Li et al. (2018) have adjusted FR to match equivalent radar reflectivity factors. Although the resulting FR are very similar (Li et al. 2018), the main difference of the methods is that snowflakes of different sizes are weighted differently in the regression process. To be consistent with a definition of FR,

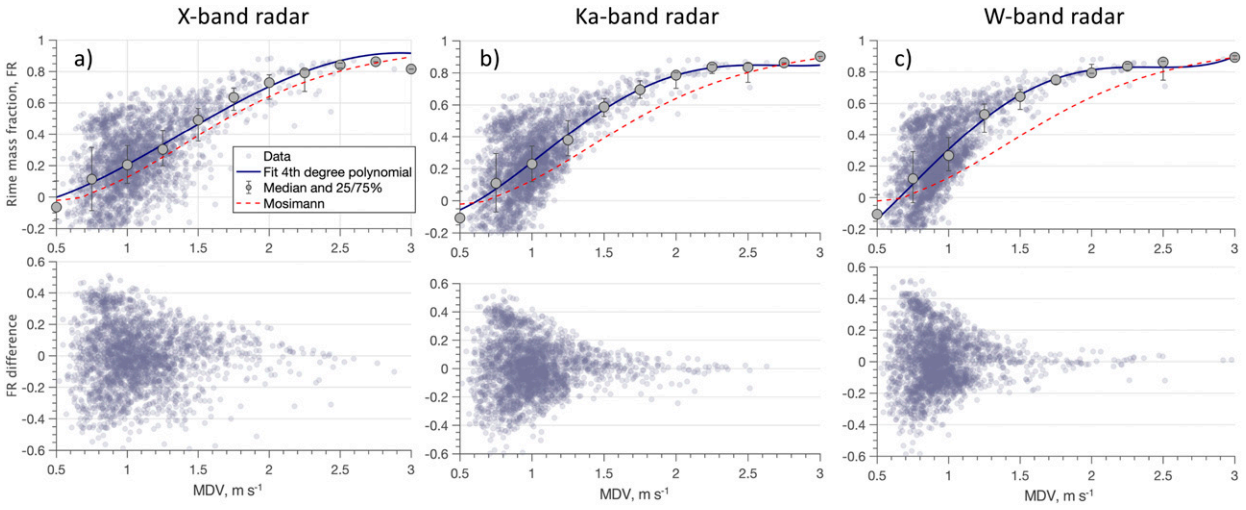

FIG. 1. (top) The relation between the rime mass fraction (FR) and mean Doppler velocity (MDV) computed for (a) X, (b) Ka, and (c) W bands. Also included are the polynomial fits (blue solid line) and Lin et al. (2011) modification of the Mosimann (1995) relation (red dashed line). (bottom) Residuals of the FR–MDV polynomial fits. Coefficients for the polynomial fits are provided in Table 1.

which is commonly used in microphysical schemes, we derive FR as follows:

$$\mathrm{FR} = 1 - \frac{\mathrm{IWC}_{\mathrm{us}}}{\mathrm{IWC}} = 1 - \frac{\int m_{\mathrm{us}}(D_{\max}) N(D_{\max})\, dD_{\max}}{\int m(D_{\max}) N(D_{\max})\, dD_{\max}}. \quad (3)$$

Here, IWC is the ice water content and the integration is implemented as a summation over in situ measured $N(D_{\max})$ and $m(D_{\max})$. Rather than using a power-law fit to measured $m(D_{\max})$, we use mean particle masses for a given size. The snowflake masses were retrieved as described in von Lerber et al. (2017), where dependence of particle terminal fall velocity on mass, size, and shape Mitchell and Heymsfield (2005) was used to retrieve ice particle masses.

Mosimann (1995) used observations of vertically pointing X-band Doppler radar in combination with Formvar replicas of ice particles on a mountain slope to derive a relation between and empirically defined degree of riming and mean Doppler velocity (MDV). The observations were taken in the Swiss Alps at 1.5 km above sea level. Therefore, to be applicable at other altitudes, a correction for air density is needed. Furthermore, the derived relation can only be applied to radar measurements at X band. It is expected that for cloud radars the connection between MDV and FR will be different due to the increasing impact of non-Rayleigh scattering at higher frequencies.

We derive the FR–MDV relation from data collected in Finland during two winter periods of the years 2013/14 and 2014/15. The MDV as it would be measured at a certain altitude with the air density ρ can be computed from the surface snowfall observations as

$$\mathrm{MDV} = \left(\frac{\rho_0}{\rho}\right)^{0.4} \frac{\int v(D_{\max}) \sigma_\lambda(D_{\max}) N(D_{\max})\, dD_{\max}}{\int \sigma_\lambda(D_{\max}) N(D_{\max})\, dD_{\max}}, \quad (4)$$

where ρ_0 is the air density at the mean sea level. The dependence of MDV on radar wavelength λ is a result of the wavelength dependence of the radar cross section $\sigma_\lambda(D_{\max})$. Similar to Eq. (3), the computations are carried out by using PSD and particle fall velocity as measured by the video imager (Newman et al. 2009; von Lerber et al. 2017). In recent studies (e.g., Tyynelä et al. 2011; Leinonen et al. 2012; Kneifel et al. 2016; Falconi et al. 2018; Schrom and Kumjian 2018), it was shown that the soft-spheroid ice particle model and corresponding T-matrix scattering computations may lead to significant errors. To avoid these errors, the single particle scattering datasets of Leinonen and Szyrmer (2015), Leinonen and Moisseev (2015), and Tyynelä and von Lerber (2019) were used. These datasets were combined in a lookup table of particle scattering properties as a function of m and $D_{\max}$. For a given m and $D_{\max}$, the backscattering cross section is estimated by using linear interpolation in the log-log space. The results of these computations are shown in Fig. 1. Note that the MDV of the Mosimann relation (Mosimann 1995; Lin et al. 2011) was converted to the mean sea level equivalent MDV.

The relation between FR and MDV was approximated by a fourth-degree polynomial of the form

$$\mathrm{FR} = p_1 \mathrm{MDV}^4 + p_2 \mathrm{MDV}^3 + p_3 \mathrm{MDV}^2 + p_4 \mathrm{MDV} + p_5. \quad (5)$$

The coefficients p_1 to p_5 of the fit are given in Table 1. As can be seen in Fig. 1, the polynomial fit for X band is quite similar to the original Mosimann relation. At higher frequencies, the differences increase and our new fit results in higher FR values for the same MDV.

At MDV between 0 and 1 m s^{-1}, there is an intrinsic ambiguity between terminal fall velocity and FR, which also explains the relatively big spread of derived FR in this region. In this velocity region, the terminal velocity of unrimed aggregates still increases with size which means that a large unrimed aggregate may have a similar velocity as a small heavily rimed

TABLE 1. Coefficients of the FR–MDV polynomial fit [Eq. (5)] for X, Ka, and W bands shown in Fig. 1, and additionally for Ku band and frequencies where all rimed particles can be assumed to scatter in the Rayleigh regime (e.g., C or S band). Positive MDV are assumed for motions toward the radar.

	p_1	p_2	p_3	p_4	p_5
Rayleigh	−0.0528	0.2927	−0.6125	1.056	−0.4691
X band	0.0095	−0.1412	0.4669	−0.0567	−0.0725
Ku band	−0.0915	0.524	−1.109	1.518.	−0.6199
Ka band	0.0791	−0.5965	1.362	−0.5525	−0.0514
W band	0.0961	−0.6073	1.032	0.2212	−0.4358

crystal (Li et al. 2018). Given that the definition of unrimed particles and corresponding mass–dimensional relation is statistical, the negative values of FR appear in cases where observed ice particle masses are smaller than defined by Eq. (2).

At velocities around 2 to 2.5 m s^{-1}, the FR–MDV relation seems to reach saturation. Although the two winter periods contain a number of graupel cases, their relative frequency is low and the dataset is dominated by lightly to moderately rimed particles. Another reason for the saturation might be the fact that the amount of rime mass has to strongly grow in order to further increase FR. As a result, even if MDV is strongly increasing due to added rimed mass, the effect on already large FR might be small.

b. Application to long-term CloudNet datasets

The new FR–MDV relation has been applied to ground-based remote sensing data processed with the CloudNet algorithm (Illingworth et al. 2007). The CloudNet data products contain the original cloud radar moments as well as a derived classification (e.g., clear sky, ice, rain, melting ice) stored on a regular grid (usually 30 s in time and 30 m in the vertical) in a standardized data format. In addition, the CloudNet products also incorporate thermodynamic variables such as temperature, pressure, or wind, which are taken from weather prediction model analysis. As discussed in the introduction, Mosimann's approach requires that the measured MDV are similar to the ice particle terminal velocities and that the contribution of vertical air motions is negligible. The most common reasons for such vertical motions are orographically induced, wavelike wind patterns, turbulent motions and gravity waves, and up- and downdrafts caused by convection. We will describe in the following how we processed and filtered the data to minimize the impact of vertical winds.

For our study, we selected four CloudNet sites from central and northern Europe (Table 2). Sites which might be strongly affected by their surrounding orography have been excluded in order to avoid biases in the retrieved FR due to persistent up- or downward motions. For central Europe, we use data from the Meteorological Observatory of the German Weather Service in Lindenberg (LIN; Görsdorf et al. 2015) and the Jülich Observatory for Cloud Evolution [JOYCE (JUE); Löhnert et al. 2015], which provide multiyear and almost continuous data records. While LIN and JUE can be seen as a representation of polluted, continental European conditions, the observations from Mace Head (MHE; Preißler et al. 2016) at the west coast of Ireland provide data for a very clean, maritime environment. Finally, the shorter dataset available from Sodankylä (SOD; Hirsikko et al. 2014), allows a comparison of midlatitude to Arctic conditions.

The processing of the vertically pointing cloud radar data starts with the definition of an averaging box which was chosen to be 20 min in time and 100 m in the vertical (corresponding to about 3 radar range gates and 40 samples in time). At least 80% of the data contained in each box are required to be classified as ice cloud or mixed-phase cloud; only clear-sky data are accepted for the remaining 20%. The temperatures inside the box are also required to be entirely below 0°C—an additional filter criterion that is somewhat redundant as temperature is also one component of CloudNet's ice/liquid classification. Nevertheless, we keep the temperature criterion for unlikely cases of a CloudNet misclassification. The radar and thermodynamic data are then averaged for each box. Our averaging time of 20 min is close to the 25 min used in Mosimann (1995) and has been shown to be an optimal trade-off between sufficient temporal resolution and elimination of high-frequency random air motions due to turbulence or gravity waves in ice clouds (Protat and Williams 2011).

Vertical air motions due to convection are more problematic as their up- and downdrafts cannot be assumed to cancel out within our 20-min averaging window. Following the approach discussed and tested by Mosimann (1995), we calculate a convection index κ which characterizes the variability of MDV within a certain time window:

$$\kappa = \frac{|\mathrm{MDV}(z) - \overline{\mathrm{MDV}(z)}|}{\overline{\mathrm{MDV}(z)}}. \tag{6}$$

Here MDV(z) is the mean Doppler velocity in the original temporal resolution and $\overline{\mathrm{MDV}(z)}$ is the average Doppler

TABLE 2. Overview of location and data periods used from four selected CloudNet sites. The radar data used by CloudNet have been collected at all sites with similar Ka-band cloud radar systems (Görsdorf et al. 2015). Data availability is defined as ratio of time periods with valid CloudNet data to the total time period.

	Jülich (JUE)	Lindenberg (LIN)	Mace Head (MHE)	Sodankylä (SOD)
Latitude	50.91°N	52.21°N	53.33°N	67.37°N
Longitude	6.41°E	14.12°E	9.90°W	26.62°E
Altitude (MSL)	111 m	104 m	16 m	171 m
Years analyzed	2010–18	2007–18	2009–18	2012–14
Data availability	69%	79%	42%	48%

velocity in the box. If we assign positive MDV to motions toward the radar, negative κ values indicate updraft regions. Following the suggestions by Mosimann (1995), we exclude all boxes which comprise mean κ values which are negative or larger than 0.2. We also tested the sensitivity of our results when filtering our datasets with a more restrictive κ of 0.1 or a more relaxed value of 0.4 and found only small changes in our statistics. Our explanation for this low sensitivity of our results to the convection filter is that our dataset is mainly dominated by stratiform clouds and only a small portion (larger during summer) is affected by convection. Also, if the convection is only moderate, we can assume that the cancellation of up- and downward motion is still sufficient to not severely disturb the riming signal.

Before applying the MDV–FR relation to the dataset, we have to correct the MDV to surface pressure conditions. This is needed as the MDV–FR relation has been derived at the ground and is hence only valid for average surface pressure. Due to lower air density higher up in the atmosphere, the ice particles will fall with a larger terminal velocity than close to the surface. This is also true for the original MDV–degree of riming relation presented in Mosimann (1995) which is only valid for a height of 1500 m MSL. To correct the MDV(z) measured at various heights z and pressure levels $p(z)$ to surface pressure level p_s we applied the correction suggested in Heymsfield et al. (2013), which was also used in Eq. (4):

$$\mathrm{MDV}_s(z) = \mathrm{MDV}(z)\left[\frac{p(z)}{p_s}\right]^{0.4}. \tag{7}$$

The average surface pressure p_s assumed for the derivation of the MDV–FR relation is 1000 hPa; $\mathrm{MDV}_s(z)$ is the pressure corrected mean Doppler velocity.

An example for the derived FR after all filtering and averaging steps have been applied is shown in Fig. 2. In this winter case observed at the JUE site, the melting layer is close to the surface. Note, that the radar data are plotted with the original resolution as stored in CloudNet (30 s, 30 m). The FR shown as black contour lines in Fig. 2b coincides with the larger area of enhanced MDV between 0500 and 0700 UTC at altitudes up to 2 km. Interestingly, the region of these enhanced MDV does not correspond to the area of enhanced reflectivities found later between 0800 and 1000 UTC. Although one can expect more dense particles to produce also larger reflectivities, the example shown in Fig. 2 clearly shows that this is not necessarily always the case. Probably, in this case, the reflectivities in the later period are enhanced by large snowflakes. This example also demonstrates that the applied averaging and filtering methods successfully exclude more ambiguous regions from the FR analysis, such as the rapidly changing positive and negative MDV in the upper part of the cloud (indicated as black diamonds in Fig. 2b).

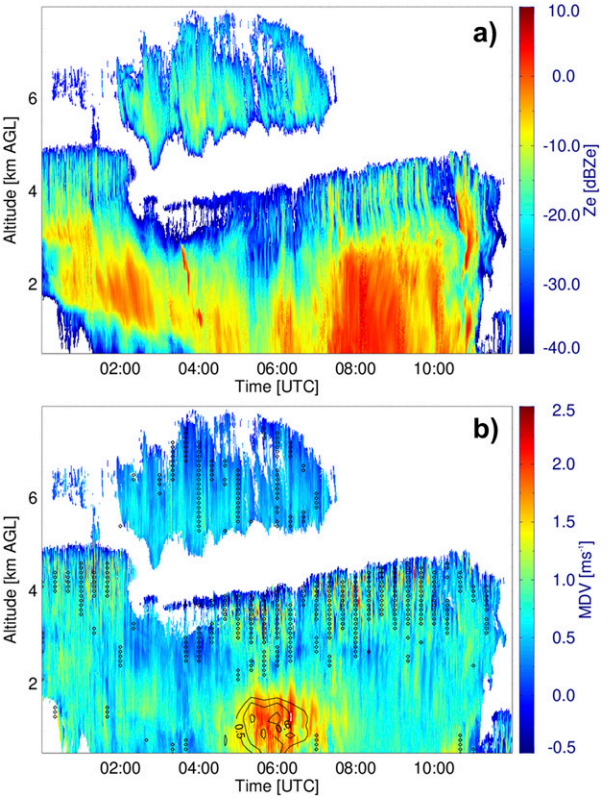

FIG. 2. (a) Radar reflectivity factor Ze and (b) mean Doppler velocity MDV of a riming case recorded on 19 Feb 2016 by the vertically pointing Ka-band cloud radar at JOYCE site (JUE). Positive MDV values denote motions toward the radar. The radar data are displayed in the original resolution (30 s, 30 m) as available from CloudNet. The black contour lines in (b) indicate the derived rime mass fraction using analysis boxes of 20 min and 100-m range (details described in the text). The black diamonds denote boxes for which the convection parameter κ exceeds the thresholds indicating updrafts, convection, or high-turbulence areas.

3. Results and discussion

a. *Riming at different sites and seasons*

Before looking specifically into statistics of riming, we first analyze the seasonal occurrence frequency of all ice clouds at the different sites. We define the frequency of ice clouds as the number of atmospheric columns (20-min temporal spacing) which contain at least one box with ice or mixed-phase clouds normalized by the total number of columns (also including, e.g., clear-sky periods). This means that our ice cloud frequency does include nonprecipitating cirrus as well as precipitating systems. Note that analysis boxes which exceed the convection index κ [see Eq. (6)] are not included in this statistics.

The three midlatitude sites show an ice cloud frequency between 10% and 40% with a slight minimum during summer (Fig. 3). At the Arctic site (SOD), the ice cloud frequency reaches values up to 50% but also shows larger variability. The larger frequency of ice clouds in the Arctic as well as the average value of 30% for the midlatitude sites are overall consistent with satellite derived values of ice cloud fraction (e.g., Matus and L'Ecuyer 2017). The lower frequency of ice containing columns during summer can be explained by the more likely presence of pure liquid clouds (e.g., shallow convection,

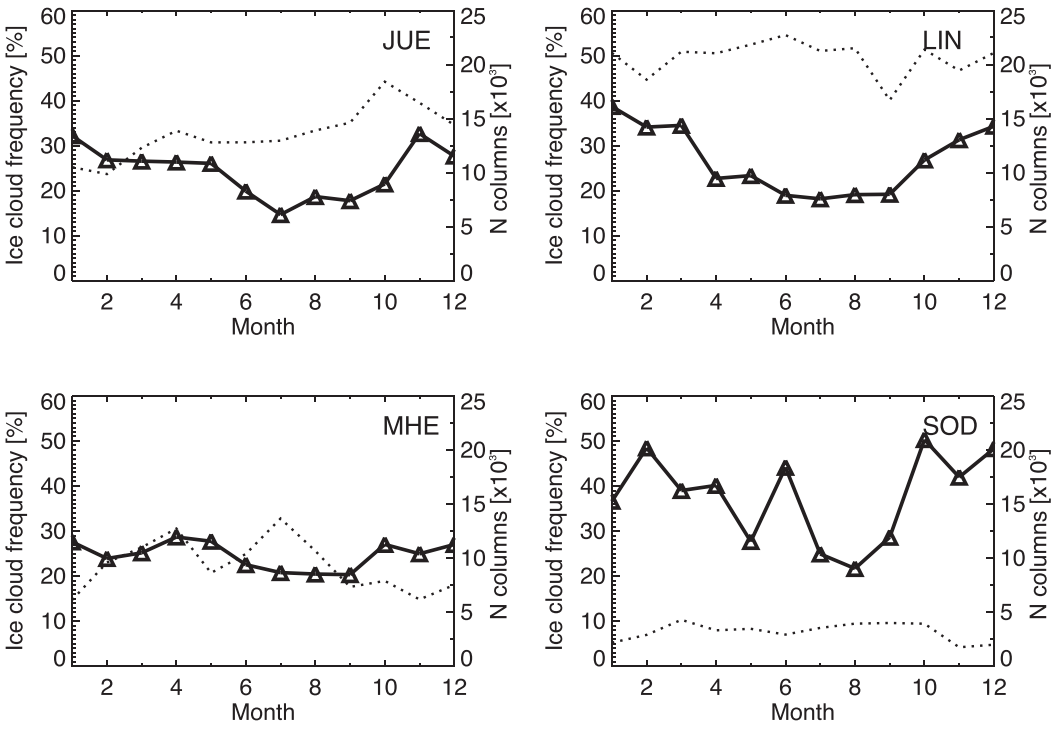

FIG. 3. Frequency of ice or mixed-phase clouds in the vertical column classified by the CloudNet algorithm (solid line; left axis) relative to the total number of columns (dashed line; right axis) at JOYCE (JUE), Lindenberg (LIN), Mace Head (MHE), and Sodankylä (SOD). Note the lower amount of data due to shorter available time periods for SOD site (see also Table 2).

boundary layer clouds) simply due to the warmer temperatures during summer (Fig. 4).

The variability of temperature over the year for the different sites is likely to affect the frequency of ice clouds but, as will be shown later, is also related to the frequency of riming. Hence, we analyzed for all sites the monthly temperature at the lowest analyzed height (~500 m above ground to ensure that the data are free of ground clutter contamination). The temperature distributions for JUE and LIN are very similar which is expected given their similar latitude and central European climatic region (Fig. 4). As expected for a site directly at the coast, MHE shows much smaller overall temperature variability and milder temperatures during winter. Temperatures at the Arctic site are overall colder and constantly below 0°C during winter and early spring. The low temperatures at SOD explain the high frequency of ice clouds during winter where the relative ice cloud frequency becomes identical to the total cloud frequency during that time (not shown).

In the next step, we only consider ice containing columns, i.e., columns where CloudNet classified at least one box as ice or mixed phase. For these columns, we determine whether the FR in at least one box within this column is larger than 0.5 (corresponding to an average mean Doppler velocity exceeding 1.4 m s^{-1}). The overall likelihood to find rimed particles with FR exceeding 0.5 in ice containing clouds ranges between 1% and 8% (Fig. 5). There is no common seasonal dependence of the riming frequency for the different sites. JUE and SOD show slightly more frequent riming during summer, while MHE shows the opposite, a minimum of riming frequency in summer and the maximum being found in winter. MHE reveals in general the largest seasonal variability of riming frequency. In contrast, LIN shows an almost constant low frequency of riming of around 3% throughout the year.

While we focused on the maximum FR in the column for determining the frequency of riming, we analyze in Fig. 6 also the distribution of the intensity of riming in terms of FR. We note again that our statistics of FR are limited to moderate riming situations with FR in the range between 0.5 and 0.86. Surprisingly, the median FR for all sites ranges between 0.5 and 0.6 with very little seasonal variation. Although riming was found to be less frequent in LIN than in JUE (Fig. 5), the distribution of FR seems to be overall very similar. Also for MHE, the strong variations of riming frequency over the year seem to be only weakly correlated with the seasonal distribution of FR.

Slightly larger differences between seasons and sites are found for the extreme FR shown in the 95th percentiles. Extreme FR up to our maximum retrievable FR of 0.86 are more frequently found in JUE and LIN than at MHE or SOD. In JUE and LIN, extreme FR also seem to be less frequent during autumn and winter. At MHE, FR exceeding 0.8 are found to be slightly less frequent when compared to JUE and LIN. At the Arctic site (SOD), we find a more pronounced seasonal dependence with larger mean and extremes of FR

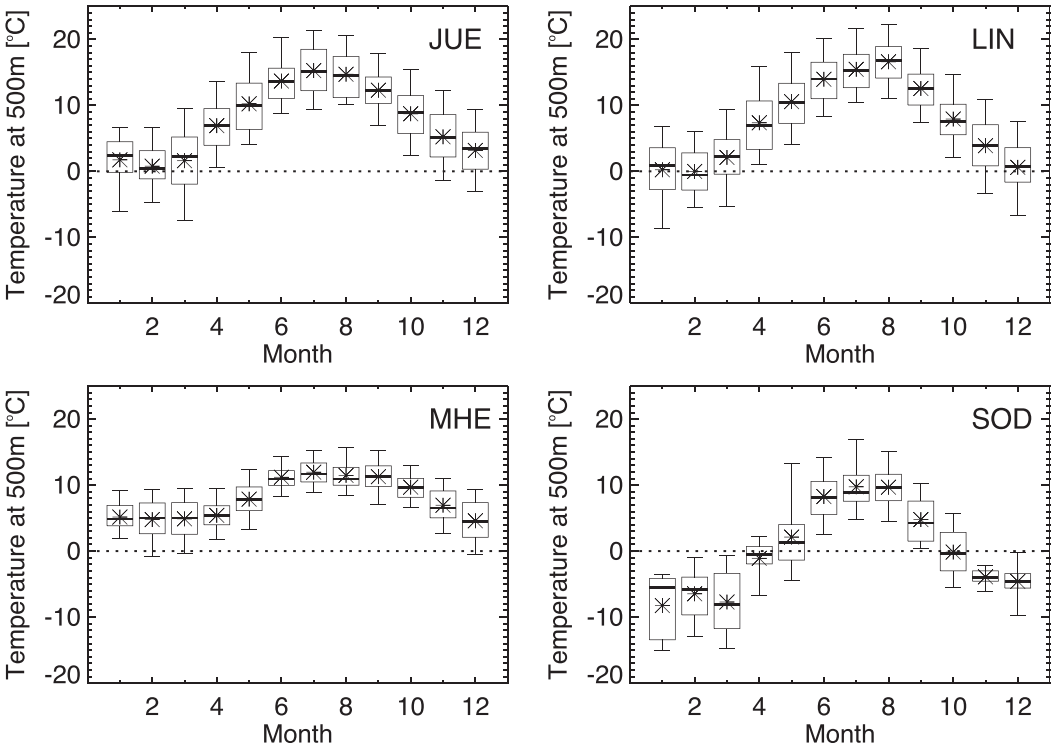

FIG. 4. Seasonal variation of air temperature (based on model analysis fields stored in the CloudNet) at the lowest analyzed height of 500 m above ground for the four sites (site abbreviations as in Fig. 3). The box encloses the quartiles, with the dash inside the box representing the median and the asterisk being the mean. Whiskers indicate the 5th and 95th percentiles.

during summer and low FR during spring and autumn. However, the statistics for SOD need to be interpreted with care due to the much smaller number of data. The weak seasonal dependence of both, the riming frequency and FR for all sites, might be a result of excluding convective cases for which much more intense FR can be expected.

b. Dependence of riming on temperature

The relatively weak seasonal dependence found in the previous section motivated us to investigate the relation of riming to other relevant variables available in the CloudNet dataset. Obviously, we expect a close relation of liquid water content (LWC) and riming. However, riming periods typically occur during times of precipitation at the surface and therefore the liquid water path retrieved from the microwave radiometer is unreliable. Even without any rain or melting particles present, we would still miss the information about the vertical distribution of liquid water within the cloud. For example, the ceilometer can only detect the lower boundary of a liquid layer.

Instead, we analyze the observations from all seasons together whether a relation between riming and temperature can be found. Although SLW is commonly found down to −38°C, we expect in general to find SLW more frequent and also in larger amounts at increasing temperatures (Korolev et al. 2003). Also the number of ice particles is expected to be smaller at higher temperatures due to increasing aggregation and lower nucleation rates. A smaller number of ice particles, which potentially grow at the expense of supercooled droplets due to the Wegener–Bergeron–Findeisen process (e.g., Korolev 2007), further increases the likelihood for SLW. Finally, the commonly observed increase of reflectivity toward the melting layer indicates a progressive growth by aggregation. Those larger snowflakes with their enhanced terminal velocities and larger cross-sectional area might favor the accretion of supercooled droplets.

Similar to the seasonal analysis, we first investigate the relative frequency of boxes classified as ice or mixed phase as function of temperature for the different sites regardless of whether they contain rimed particles (Fig. 7). Within the temperature range from −1° to −40°C, where we can expect SLW to coexist with ice particles, we find 10% to 28% of the boxes filled with ice or mixed-phase clouds. Interestingly, the differences between the midlatitude sites is again very small, while the Arctic site shows slightly larger values throughout the entire temperature range. All sites (except MHE) also show a small maximum in ice cloud frequency between −5° and −15°C.

The boxes containing ice or mixed-phase particles are then analyzed with respect to their FR. First, we calculate the frequency of FR exceeding our threshold of 0.5 as done before in the seasonal analysis. By dividing this number of rimed boxes by the number of ice and/or mixed-phase boxes for each temperature bin, we obtain the relative riming frequency as function of temperature (Fig. 8). At all sites, we find a steep

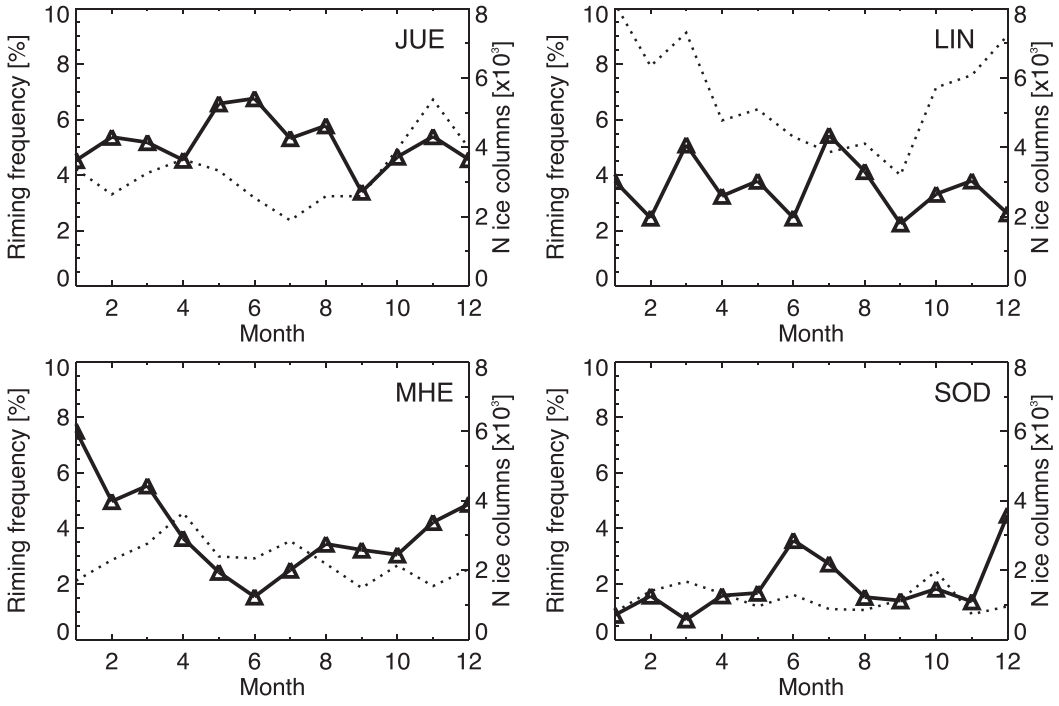

FIG. 5. Frequency of riming (solid line; left y axis) defined as FR > 0.5 in the column relative to the total number of columns containing ice or mixed phase (dashed line; right y axis) according to the CloudNet categorization. Site abbreviations are as in Fig. 3.

increase of the frequency of moderate to heavy riming if temperatures become larger than −12°C. Even at the Arctic site (SOD), the likelihood to find FR larger than 0.5 at lower temperatures in nonconvective clouds is below 1%. The maximum frequency of riming reaches values between 6% and 14% at a temperature close to 0°C. There are small differences between the sites with JUE showing the largest frequency of riming followed by MHE and LIN; the lowest frequency of riming is found for SOD which also shows a small plateau around −5°C.

The temperature dependence of riming shown in Fig. 8 looks astonishingly similar to the temperature dependence of the occurrence of freezing drizzle and rain presented in Cortinas et al. (2004) (their Fig. 12). It seems quite plausible that the temperature dependence of riming frequency is strongly related to the presence of supercooled drizzle or rain. Those relatively large supercooled drops are much more efficient in colliding with ice particles and will also cause the riming process to be much faster than for the mass equivalent amount of smaller drops. Besides the more frequent occurrence of larger supercooled drops at higher temperatures, simulation studies for the phase transition within mixed-phase clouds also found a strong temperature dependence of SLW. In Fig. 12a of Pinsky et al. (2015), the simulated maximum LWC is shown as function of temperature for different ice number concentrations varying from 0.5 to 2 L^{-1}. The curves show a very steep increase of LWC at −12°C which further increases toward higher temperatures. Also aircraft observations of various kinds of mixed-phase clouds indicate a strong increase (almost one order of magnitude) of LWC at temperatures larger than −18°C while ice water contents are relatively constant between −30° and −2°C (see, e.g., Fig. 7 in Korolev et al. 2003).

In addition to the strong temperature dependence of LWC and droplet size, the size and morphology of the collecting ice particles also changes with temperature. Riming of single crystals strongly depends on their habit (Jensen and Harrington 2015), which is mainly determined by temperature and supersaturation (Bailey and Hallett 2009). Under sufficient supersaturated conditions, ice particles grow at temperatures close to −15°C preferably into dendritic crystals. Due to their branched structure, dendrites show an enhanced sticking efficiency (Connolly et al. 2012), which is assumed to be the main reason for the frequently observed rapid increase in aggregation and mean particle size at this temperature (e.g., Barrett et al. 2019; Dias Neto et al. 2019; among others). As aggregates tend to be more efficient in riming than single crystals (Lew et al. 1986; Wang and Ji 2000), this enhancement of aggregation close to −15°C might be an additional factor for the rapidly increasing riming frequency.

Considering the increase of LWC and droplet size with higher temperatures, we might also expect FR to be more intense at rising temperatures. We investigate this aspect in Fig. 9, where we look at average and percentiles of FR for temperatures above −12°C (lower temperatures have been excluded because the number of cases with FR > 0.5 are very few). Surprisingly, FR is fairly constant across the temperature range with median values between 0.5 and 0.6. Even the extreme FR (95th percentiles) seem not to show an increase with

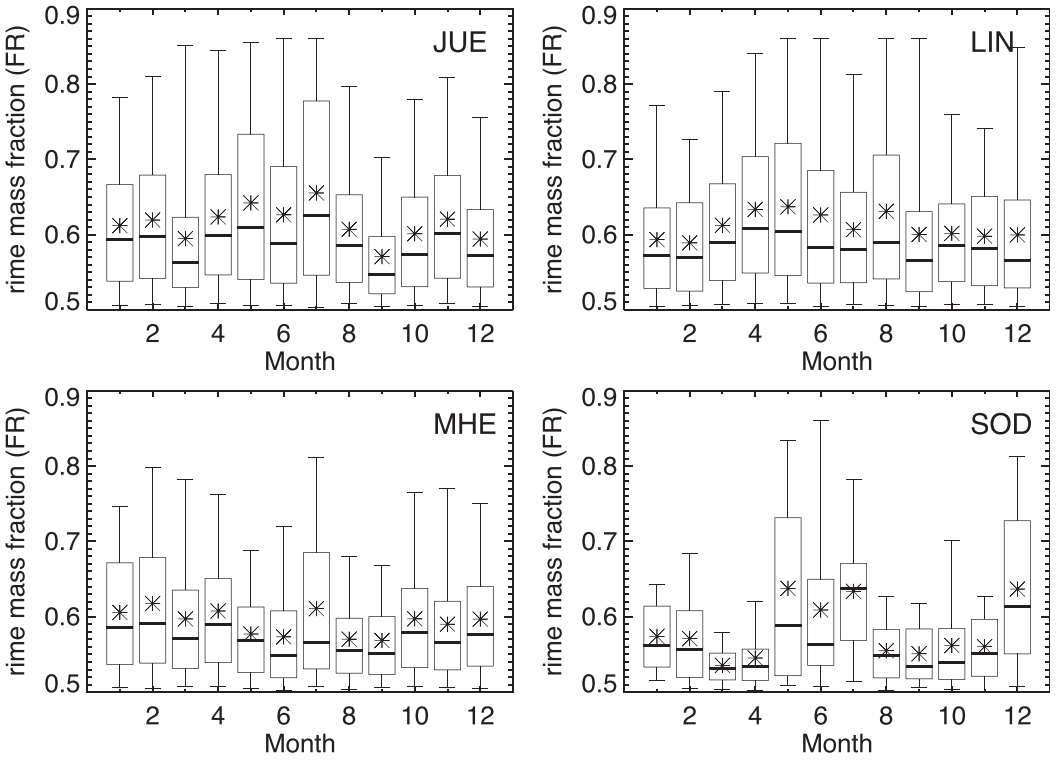

FIG. 6. Seasonal variability of observed rime mass fraction for the different sites. Site abbreviations are as in Fig. 3. The definition of box and whiskers are as in Fig. 4. Note that the minimum (maximum) rime mass fraction in the retrieval is limited to 0.5 (0.86).

temperature as we might have expected from Fig. 8. We can only speculate why the FR is rather temperature independent. One hypothesis is that the snowflakes grow to larger sizes when falling closer to the 0°C level, for example, due to increasing sticking efficiency (Lamb and Verlinde 2011). Larger snowflakes might also need a much larger amount of SLW to reach the same FR as compared to smaller aggregates further up in the cloud. The variability of the FR for the different sites is again very similar to what we found for the seasonal dependence (Fig. 6) with MHE and SOD showing lower extreme FR as compared to JUE and LIN.

As mentioned in the introduction, the number of aerosols is also expected to play a key role for riming. In a more polluted environment, we would in general expect the liquid water to be distributed over a larger number of smaller sized drops. As the efficiency of riming is strongly decreasing with smaller drop size (Wang and Ji 2000), one would expect less riming in regions with high aerosol loading. Only very few observational studies exist, which investigated this effect. Borys et al. (2003) studied two case studies of orographic snowfall with combined in situ and remote sensing observations [riming was quantified using the approach by Mosimann (1995)]. The two cases had similar liquid water contents but very different aerosol loading. The supercooled drop spectra showed the expected difference in size distribution and riming was found to be inhibited for the polluted case. Although we did not include any detailed aerosol measurements for this analysis, we can generally assume the aerosol loading for MHE to be substantially lower as compared to JUE. In fact, the location of MHE site was specifically chosen to provide measurement with very limited anthropogenic influence (O'Connor et al. 2008). However, neither riming frequency nor FR show the expected enhancement for MHE.

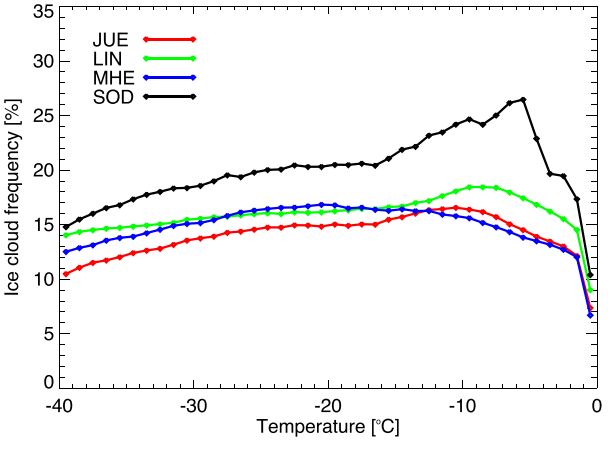

FIG. 7. Frequency of ice or mixed-phase clouds according to the Cloudnet categorization relative to the total number of observations (including clear-sky boxes) for 1°C temperature bins and the four different sites: JUE (red), LIN (green), MHE (blue), and SOD (black).

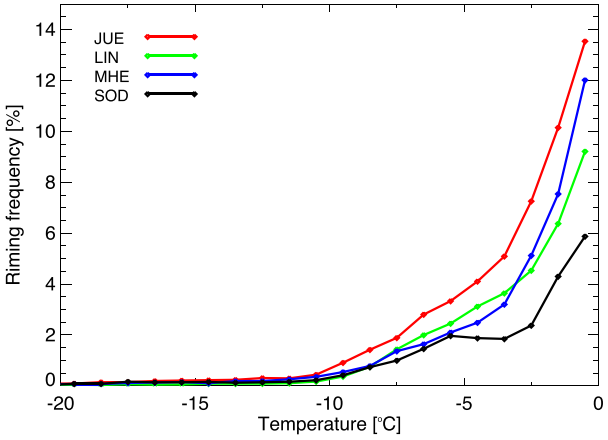

FIG. 8. Frequency of riming defined as FR > 0.5 for each temperature bin relative to the total number of boxes containing ice or mixed phase according to the CloudNet categorization. Color coding and site abbreviations are as in Fig. 7.

On the contrary, the results shown in Figs. 5 and 6 indicate rather the opposite, a lower frequency and FR for MHE as compared to JUE or LIN. As pointed out by Lohmann et al. (2003), the shape of the ice particles plays a crucial role for the riming process. In their simulation study, Lohmann et al. (2003) found for a tenfold increase in aerosol concentration an increase of snow on the ground by 40% when assuming aggregates but a 30% decrease for planar crystals. This might explain some of the discrepancy between the results in Borys et al. (2003) and our study. The snow falling from the two low level clouds in Borys et al. (2003) where mostly planar dendrites. For our statistics at the midlatitude sites, the majority of detected riming cases is connected to deep frontal clouds. In the temperature regime, where we find riming to be most frequent (increasing from −12° to 0°C), we also expect aggregates to be the dominant particle types. According to Lohmann et al. (2003), a larger number of supercooled drops accrete on aggregates for higher aerosol concentrations, which could at least partly explain lower riming at MHE compared to JUE and LIN. Certainly, more combined observational studies of collocated aerosol and cloud property measurements including different cloud regimes are needed in order to better understand the aerosol influence on riming.

4. Summary and conclusions

In this study, we revisited a previously published relation between the rime mass fraction (FR) and the mean Doppler velocity (MDV) measured by ground-based, vertically pointing radar. Relations between FR and mean Doppler velocity applicable to X-, Ka-, and W-band measurements have been derived using a large dataset of in situ snow measurements from Finland. Our relation compares well with the original

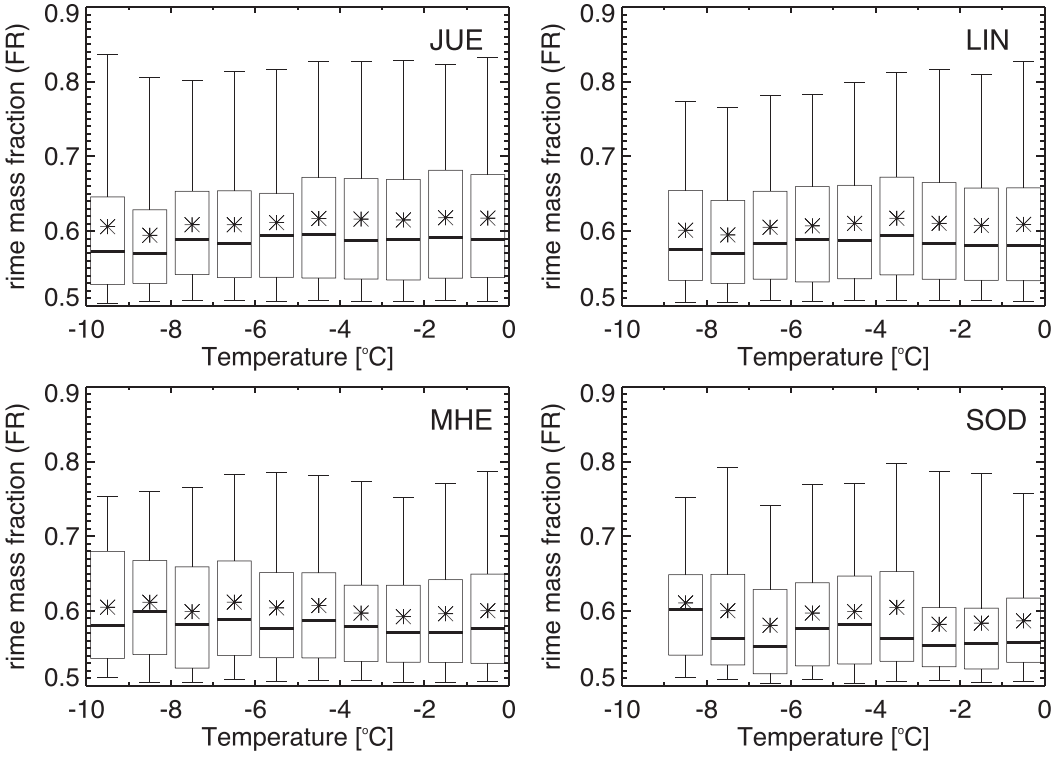

FIG. 9. Dependence of rime mass fraction on temperature for the different sites. Site abbreviations are as in Fig. 3. The definition of box and whiskers are as in Fig. 4. Note that the minimum (maximum) rime mass fraction in the retrieval is limited to 0.5 (0.86).

relation, which was based on a much smaller amount of data and which was only applicable to X-band radars.

The new riming relation has been applied to CloudNet products generated with multiyear radar datasets from four European sites covering Germany, Ireland, and northern Finland (Arctic) representing different climatic and aerosol conditions. As the method relies on a realistic estimate of the terminal fall velocity of the ice particles measured by a radar, several filtering steps have been applied in order to minimize disturbing effects due to turbulence and gravity waves. In addition, convective cases have been widely eliminated as their up- and downdrafts can deteriorate the estimates of FR.

The terminal velocities of unrimed ice and snow particles at surface pressure conditions are usually reaching a saturation value of around $1\,m\,s^{-1}$. Hence, Doppler velocities up to this value cannot be used to derive FR. We therefore limited our analysis to Doppler velocities larger than $1.4\,m\,s^{-1}$, which corresponds to a FR of 0.5 and which we can reliably relate to moderately rimed particles.

We investigated the relative frequency as well as the distribution of FR for different months and as function of in-cloud temperature for all sites. The seasonal variability of the riming frequency is in a similar range as the variation found for different sites. Considering an atmospheric column which contains ice or mixed-phase cloud, we find the likelihood for FR to exceed 0.5 to range between 1% and 8%. The median FR for different months and sites is also surprisingly similar and ranges between 0.5 and 0.6. The two German sites show overall the largest extreme values of FR. If at all recognizable, the correlation between riming frequency and FR is very weak.

We found the most surprising signature when we analyzed the frequency of riming as function of cloud temperature (Fig. 8). The frequency of riming steeply increases for all sites at temperatures larger than −12°C. The largest frequency of riming is found close to 0°C with values ranging between 6% for the Arctic site and 9%–14% for the midlatitude sites. It appears to be very likely that the temperature dependence of riming frequency is connected to the strong increase of the amount of SLW and/or larger droplet sizes found in previous observational and modeling studies for temperatures larger than −12°C. If this link can be confirmed by future studies, our statistical approach to determine riming frequency and FR using cloud radars could also be used to derive information on the probability of aircraft icing conditions. Although the SLW itself is problematic to directly detect by radar, it is closely connected to the presence of a riming signature and can thus be reliably detected at many sites.

However, the nonexisting temperature dependence of FR (Fig. 9) is a result that we are unable to explain at the moment. We imagine that the general increase of aggregation and therefore also snowflake size toward the freezing level might compensate the increasingly available SLW. Larger snowflakes will simply need more SLW to reach the same FR as smaller aggregates which might explain the overall similar FR within 0° and −10°C.

Although the statistics in this study are lacking sufficient information on aerosols, we find for the cleaner environment at MHE less riming than for the two continental and more polluted sites (JUE and LIN). This seems to be in contradiction to previous case studies (Borys et al. 2003), where larger aerosol concentrations caused a larger number of smaller sized supercooled drops, which seemed to inhibit riming. We hypothesize that the high sensitivity of riming to ice particle shape might at least partly explain this discrepancy, which seems to be confirmed by simulation studies (Lohmann et al. 2003; Lohmann 2004). A further development of previous laboratory studies (Lew et al. 1986; Wang and Ji 2000) and field experiments appears to be highly necessary in order to better understand the impact of ice particle properties, liquid droplet size, and aerosols on riming. An improved understanding of riming is particularly relevant for convective clouds where rimed particles are often the precursor of hail.

We expect our statistics of frequency of riming and rime mass fraction to be valuable for evaluating and further developing riming parameterizations in models. Examples for such developments have been given in Lin et al. (2011) for bulk models. New modeling approaches, such as the new predicted particle properties (P3; Morrison and Milbrandt 2015) scheme, provide in particular substantial improvements regarding rimed particles. Their prediction of riming related variables, such as rime mass, will allow to compare directly retrieved quantities as FR with model output. In addition, Lagrangian superparticle models (Brdar and Seifert 2018; Seifert et al. 2019) provide the evolution of rimed particles in high detail, which opens up new opportunities to compare with observations.

Also, new observational capabilities, such as the upcoming EarthCARE mission (Illingworth et al. 2015) with its first W-band Doppler radar in space will provide unprecedented opportunities to investigate riming on a global scale in addition to the long-term observations of ground-based sites. Ground-based observatories should also further explore synergies of multifrequency radar approaches, Doppler measurements, and polarimetry for quantifying riming over the entire range of observed FR and to also develop approaches how riming can better retrieved in convective clouds.

Acknowledgments. This study and all contributions by SK have been funded by the German Research Foundation [Deutsche Forschungsgemeinschaft (DFG)] under Grant KN 1112/2-1 as part of the Emmy-Noether Group OPTIMIce. DM was supported by the Academy of Finland Finnish Center of Excellence program (Grant 307331) and ERA-PLANET, transnational project iCUPE (Grant Agreement 689443), funded under the EU Horizon 2020 Framework Programme. We especially acknowledge the enormous efforts of the responsible technicians and scientists at the four research sites for collecting high-quality long-term radar observations and for providing their data to CloudNet. All data for this study have been obtained through the CloudNet data portal (http://devcloudnet.fmi.fi/). We acknowledge the ACTRIS-2 project (European Commission Contract H2020-INFRAIA, Grant 654109) for providing the target classification, which was produced by the Finnish Meteorological Institute using measurements from the four sites. Relevant data for developing the methodology were provided by DFG-funded Core

Facility (JOYCE-CF) under DFG Research Grant LO 901/7-1. We also would like to thank Bernhard Pospichal and Axel Seifert for fruitful discussions and are grateful to Ewan O'Connor for his support regarding CloudNet data access.

REFERENCES

Bailey, M. P., and J. Hallett, 2009: A comprehensive habit diagram for atmospheric ice crystals: Confirmation from the laboratory, AIRS II, and other field studies. *J. Atmos. Sci.*, **66**, 2888–2899, https://doi.org/10.1175/2009JAS2883.1.

Barrett, A. I., C. D. Westbrook, J. C. Nicol, and T. H. M. Stein, 2019: Rapid ice aggregation process revealed through triple-wavelength Doppler spectrum radar analysis. *Atmos. Chem. Phys.*, **19**, 5753–5769, https://doi.org/10.5194/acp-19-5753-2019.

Borys, R. D., D. H. Lowenthal, S. A. Cohn, and W. O. J. Brown, 2003: Mountaintop and radar measurements of anthropogenic aerosol effects on snow growth and snowfall rate. *Geophys. Res. Lett.*, **30**, 1538, https://doi.org/10.1029/2002GL016855.

Brdar, S., and A. Seifert, 2018: McSnow: A Monte-Carlo particle model for riming and aggregation of ice particles in a multidimensional microphysical phase space. *J. Adv. Model. Earth Syst.*, **10**, 187–206, https://doi.org/10.1002/2017MS001167.

Brown, P. R. A., and P. N. Francis, 1995: Improved measurements of the ice water content in cirrus using a total-water probe. *J. Atmos. Oceanic Technol.*, **12**, 410–414, https://doi.org/10.1175/1520-0426(1995)012<0410:IMOTIW>2.0.CO;2.

Colle, B. A., D. Stark, and S. E. Yuter, 2014: Surface microphysical observations within east coast winter storms on Long Island, New York. *Mon. Wea. Rev.*, **142**, 3126–3146, https://doi.org/10.1175/MWR-D-14-00035.1.

Connolly, P. J., C. Emersic, and P. R. Field, 2012: A laboratory investigation into the aggregation efficiency of small ice crystals. *Atmos. Chem. Phys.*, **12**, 2055–2076, https://doi.org/10.5194/acp-12-2055-2012.

Cortinas, J. V., Jr., B. C. Bernstein, C. C. Robbins, and J. W. Strapp, 2004: An analysis of freezing rain, freezing drizzle, and ice pellets across the United States and Canada: 1976–90. *Wea. Forecasting*, **19**, 377–390, https://doi.org/10.1175/1520-0434(2004)019%3C0377:AAOFRF%3E2.0.CO;2.

Dias Neto, J., and Coauthors, 2019: The triple-frequency and polarimetric radar experiment for improving process observations of winter precipitation. *Earth Syst. Sci. Data*, **11**, 845–863, https://doi.org/10.5194/essd-11-845-2019.

Erfani, E., and D. L. Mitchell, 2017: Growth of ice particle mass and projected area during riming. *Atmos. Chem. Phys.*, **17**, 1241–1257, https://doi.org/10.5194/acp-17-1241-2017.

Falconi, M. T., A. von Lerber, D. Ori, F. S. Marzano, and D. Moisseev, 2018: Snowfall retrieval at X, Ka and W bands: Consistency of backscattering and microphysical properties using BAECC ground-based measurements. *Atmos. Meas. Tech.*, **11**, 3059–3079, https://doi.org/10.5194/amt-11-3059-2018.

Field, P. R., and Coauthors, 2017: Secondary ice production: Current state of the science and recommendations for the future. *Ice Formation and Evolution in Clouds and Precipitation: Measurement and Modeling Challenges*, *Meteor. Monogr.*, No. 58, Amer. Meteor. Soc., https://doi.org/10.1175/AMSMONOGRAPHS-D-16-0014.1.

Garrett, T. J., and S. E. Yuter, 2014: Observed influence of riming, temperature, and turbulence on the fallspeed of solid precipitation. *Geophys. Res. Lett.*, **41**, 6515–6522, https://doi.org/10.1002/2014GL061016.

Giangrande, S. E., T. Toto, A. Bansemer, M. R. Kumjian, S. Mishra, and A. V. Ryzhkov, 2016: Insights into riming and aggregation processes as revealed by aircraft, radar, and disdrometer observations for a 27 April 2011 widespread precipitation event. *J. Geophys. Res. Atmos.*, **121**, 5846–5863, https://doi.org/10.1002/2015JD024537.

Görsdorf, U., V. Lehmann, M. Bauer-Pfundstein, G. Peters, D. Vavriv, V. Vinogradov, and V. Volkov, 2015: A 35-ghz polarimetric doppler radar for long-term observations of cloud parameters: Description of system and data processing. *J. Atmos. Oceanic Technol.*, **32**, 675–690, https://doi.org/10.1175/JTECH-D-14-00066.1.

Grazioli, J., G. Lloyd, L. Panziera, C. R. Hoyle, P. J. Connolly, J. Henneberger, and A. Berne, 2015: Polarimetric radar and in situ observations of riming and snowfall microphysics during CLACE 2014. *Atmos. Chem. Phys.*, **15**, 13 787–13 802, https://doi.org/10.5194/acp-15-13787-2015.

Hallett, J., and S. C. Mossop, 1974: Production of secondary ice particles during the riming process. *Nature*, **249**, 26–28, https://doi.org/10.1038/249026a0.

Harimaya, T., and M. Sato, 1989: Measurement of the riming amount on snowflakes. *J. Fac. Sci. Hokkaido Univ. Ser. 7*, **8**, 355–366.

Heymsfield, A. J., 1982: A comparative study of the rates of development of potential graupel and hail embryos in high plains storms. *J. Atmos. Sci.*, **39**, 2867–2897, https://doi.org/10.1175/1520-0469(1982)039<2867:ACSOTR>2.0.CO;2.

——, C. Schmitt, and A. Bansemer, 2013: Ice cloud particle size distributions and pressure-dependent terminal velocities from in situ observations at temperatures from 0° to −86°C. *J. Atmos. Sci.*, **70**, 4123–4154, https://doi.org/10.1175/JAS-D-12-0124.1.

Hirsikko, A., and Coauthors, 2014: Observing wind, aerosol particles, cloud and precipitation: Finland's new ground-based remote-sensing network. *Atmos. Meas. Tech.*, **7**, 1351–1375, https://doi.org/10.5194/amt-7-1351-2014.

Illingworth, A. J., and Coauthors, 2007: CloudNet: Continuous evaluation of cloud profiles in seven operational models using ground-based observations. *Bull. Amer. Meteor. Soc.*, **88**, 883–898, https://doi.org/10.1175/BAMS-88-6-883.

——, and Coauthors, 2015: The EarthCARE satellite: The next step forward in global measurements of clouds, aerosols, precipitation, and radiation. *Bull. Amer. Meteor. Soc.*, **96**, 1311–1332, https://doi.org/10.1175/BAMS-D-12-00227.1.

Jensen, A. A., and J. Y. Harrington, 2015: Modeling ice crystal aspect ratio evolution during riming: A single-particle growth model. *J. Atmos. Sci.*, **72**, 2569–2590, https://doi.org/10.1175/JAS-D-14-0297.1.

Kalesse, H., W. Szyrmer, S. Kneifel, P. Kollias, and E. Luke, 2016: Fingerprints of a riming event on cloud radar Doppler spectra: Observations and modeling. *Atmos. Chem. Phys.*, **16**, 2997–3012, https://doi.org/10.5194/acp-16-2997-2016.

Kneifel, S., A. von Lerber, J. Tiira, D. Moisseev, P. Kollias, and J. Leinonen, 2015: Observed relations between snowfall microphysics and triple-frequency radar measurements. *J. Geophys. Res. Atmos.*, **120**, 6034–6055, https://doi.org/10.1002/2015JD023156.

——, P. Kollias, A. Battaglia, J. Leinonen, M. Maahn, H. Kalesse, and F. Tridon, 2016: First observations of triple-frequency radar Doppler spectra in snowfall: Interpretation and applications. *Geophys. Res. Lett.*, **43**, 2225–2233, https://doi.org/10.1002/2015GL067618.

Korolev, A. V., 2007: Limitations of the Wegener–Bergeron–Findeisen mechanism in the evolution of mixed-phase clouds. *J. Atmos. Sci.*, **64**, 3372–3375, https://doi.org/10.1175/JAS4035.1.

——, G. A. Isaac, S. G. Cober, J. W. Strapp, and J. Hallett, 2003: Microphysical characterization of mixed-phase clouds. *Quart. J. Roy. Meteor. Soc.*, **129**, 39–65, https://doi.org/10.1256/qj.01.204.

Kumjian, M. R., and K. A. Lombardo, 2017: Insights into the evolving microphysical and kinematic structure of northeastern U.S. winter storms from dual-polarization Doppler radar. *Mon. Wea. Rev.*, **145**, 1033–1061, https://doi.org/10.1175/MWR-D-15-0451.1.

——, S. A. Rutledge, R. M. Rasmussen, P. C. Kennedy, and M. Dixon, 2014: High-resolution polarimetric radar observations of snow-generating cells. *J. Appl. Meteor. Climatol.*, **53**, 1636–1658, https://doi.org/10.1175/JAMC-D-13-0312.1.

——, S. Mishra, S. E. Giangrande, T. Toto, A. V. Ryzhkov, and A. Bansemer, 2016: Polarimetric radar and aircraft observations of saggy bright bands during MC3E. *J. Geophys. Res. Atmos.*, **121**, 3584–3607, https://doi.org/10.1002/2015JD024446.

Lamb, D., and J. Verlinde, 2011: *Physics and Chemistry of Clouds*. Cambridge University Press, 599 pp., https://doi.org/10.1017/CBO9780511976377.

Leinonen, J., and D. Moisseev, 2015: What do triple-frequency radar signatures reveal about aggregate snowflakes? *J. Geophys. Res. Atmos.*, **120**, 229–239, https://doi.org/10.1002/2014JD022072.

——, and W. Szyrmer, 2015: Radar signatures of snowflake riming: A modeling study. *Earth Space Sci.*, **2**, 346–358, https://doi.org/10.1002/2015EA000102.

——, S. Kneifel, D. Moisseev, J. Tyynelä, S. Tanelli, and T. Nousiainen, 2012: Evidence of nonspheroidal behavior in millimeter-wavelength radar observations of snowfall. *J. Geophys. Res.*, **117**, D18205, https://doi.org/10.1029/2012JD017680.

——, and Coauthors, 2018: Retrieval of snowflake microphysical properties from multifrequency radar observations. *Atmos. Meas. Tech.*, **11**, 5471–5488, https://doi.org/10.5194/amt-11-5471-2018.

Lew, J. K., D. C. Montague, H. R. Pruppacher, and R. M. Rasmussen, 1986: A wind tunnel investigation on the riming of snowflakes. Part II: Natural and synthetic aggregates. *J. Atmos. Sci.*, **43**, 2410–2417, https://doi.org/10.1175/1520-0469(1986)043<2410:AWTIOT>2.0.CO;2.

Li, H., D. Moisseev, and A. von Lerber, 2018: How does riming affect dual-polarization radar observations and snowflake shape? *J. Geophys. Res. Atmos.*, **123**, 6070–6081, https://doi.org/10.1029/2017JD028186.

Lin, Y., L. J. Donner, and B. A. Colle, 2011: Parameterization of riming intensity and its impact on ice fall speed using ARM data. *Mon. Wea. Rev.*, **139**, 1036–1047, https://doi.org/10.1175/2010MWR3299.1.

Lohmann, U., 2004: Can anthropogenic aerosols decrease the snowfall rate? *J. Atmos. Sci.*, **61**, 2457–2468, https://doi.org/10.1175/1520-0469(2004)061%3C2457:CAADTS%3E2.0.CO;2.

——, J. Zhang, and J. Pi, 2003: Sensitivity studies of the effect of increased aerosol concentrations and snow crystal shape on the snowfall rate in the arctic. *J. Geophys. Res.*, **108**, 4341, https://doi.org/10.1029/2003JD003377.

Löhnert, U., and Coauthors, 2015: JOYCE: Jülich Observatory for Cloud Evolution. *Bull. Amer. Meteor. Soc.*, **96**, 1157–1174, https://doi.org/10.1175/BAMS-D-14-00105.1.

Lowenthal, D. H., R. D. Borys, W. Cotton, S. Saleeby, S. A. Cohn, and W. O. Brown, 2011: The altitude of snow growth by riming and vapor deposition in mixed-phase orographic clouds. *Atmos. Environ.*, **45**, 519–522, https://doi.org/10.1016/j.atmosenv.2010.09.061.

Mason, S. L., C. J. Chiu, R. J. Hogan, D. Moisseev, and S. Kneifel, 2018: Retrievals of riming and snow density from vertically pointing Doppler radars. *J. Geophys. Res. Atmos.*, **123**, 13 807–13 834, https://doi.org/10.1029/2018JD028603.

Matus, A. V., and T. S. L'Ecuyer, 2017: The role of cloud phase in Earth's radiation budget. *J. Geophys. Res. Atmos.*, **122**, 2559–2578, https://doi.org/10.1002/2016JD025951.

Mitchell, D. L., and A. J. Heymsfield, 2005: Refinements in the treatment of ice particle terminal velocities, highlighting aggregates. *J. Atmos. Sci.*, **65**, 1637–1644, https://doi.org/10.1175/JAS3413.1.

——, R. Zhang, and R. L. Pitter, 1990: Mass-dimensional relationships for ice particles and the influence of riming on snowfall rates. *J. Appl. Meteor.*, **29**, 153–163, https://doi.org/10.1175/1520-0450(1990)029<0153:MDRFIP>2.0.CO;2.

Moisseev, D., A. von Lerber, and J. Tiira, 2017: Quantifying the effect of riming on snowfall using ground-based observations. *J. Geophys. Res. Atmos.*, **122**, 4019–4037, https://doi.org/10.1002/2016JD026272.

Morrison, H., and W. W. Grabowski, 2008: A novel approach for representing ice microphysics in models: Description and tests using a kinematic framework. *J. Atmos. Sci.*, **65**, 1528–1548, https://doi.org/10.1175/2007JAS2491.1.

——, and J. A. Milbrandt, 2015: Parameterization of cloud microphysics based on the prediction of bulk ice particle properties. Part I: Scheme description and idealized tests. *J. Atmos. Sci.*, **72**, 287–311, https://doi.org/10.1175/JAS-D-14-0065.1.

Mosimann, L., 1995: An improved method for determining the degree of snow crystal riming by vertical Doppler radar. *Atmos. Res.*, **37**, 305–323, https://doi.org/10.1016/0169-8095(94)00050-N.

——, E. Weingartner, and A. Waldvogel, 1994: An analysis of accreted drop sizes and mass on rimed snow crystals. *J. Atmos. Sci.*, **51**, 1548–1558, https://doi.org/10.1175/1520-0469(1994)051%3C1548:AAOADS%3E2.0.CO;2.

Newman, A. J., P. A. Kucera, and L. F. Bliven, 2009: Presenting the Snowflake Video Imager (SVI). *J. Atmos. Oceanic Technol.*, **26**, 167–179, https://doi.org/10.1175/2008JTECHA1148.1.

O'Connor, T., S. Jennings, and C. O'Dowd, 2008: Highlights of fifty years of atmospheric aerosol research at Mace Head. *Atmos. Res.*, **90**, 338–355, https://doi.org/10.1016/j.atmosres.2008.08.014.

Pinsky, M., A. Khain, and A. Korolev, 2015: Phase transformations in an ascending adiabatic mixed-phase cloud volume. *J. Geophys. Res. Atmos.*, **120**, 3329–3353, https://doi.org/10.1002/2015JD023094.

Praz, C., Y.-A. Roulet, and A. Berne, 2017: Solid hydrometeor classification and riming degree estimation from pictures collected with a multi-angle snowflake camera. *Atmos. Meas. Tech.*, **10**, 1335–1357, https://doi.org/10.5194/amt-10-1335-2017.

Preißler, J., and Coauthors, 2016: Six years of surface remote sensing of stratiform warm clouds in marine and continental air over Mace Head, Ireland. *J. Geophys. Res. Atmos.*, **121**, 14 538–14 557, https://doi.org/10.1002/2016JD025360.

Protat, A., and C. R. Williams, 2011: The accuracy of radar estimates of ice terminal fall speed from vertically pointing Doppler radar measurements. *J. Appl. Meteor. Climatol.*, **50**, 2120–2138, https://doi.org/10.1175/JAMC-D-10-05031.1.

Schrom, R. S., and M. R. Kumjian, 2018: Bulk-density representations of branched planar ice crystals: Errors in the polarimetric

radar variables. *J. Appl. Meteor. Climatol.*, **57**, 333–346, https://doi.org/10.1175/JAMC-D-17-0114.1.

Seifert, A., J. Leinonen, C. Siewert, and S. Kneifel, 2019: The geometry of rimed aggregate snowflakes: A modeling study. *J. Adv. Model. Earth Syst.*, **11**, 712–731, https://doi.org/10.1029/2018MS001519.

Sinclair, V. A., D. Moisseev, and A. von Lerber, 2016: How dual-polarization radar observations can be used to verify model representation of secondary ice. *J. Geophys. Res. Atmos.*, **121**, 10 954–10 970, https://doi.org/10.1002/2016JD025381.

Tyynelä, J., and A. von Lerber, 2019: Validation of microphysical snow models using in-situ, multi-frequency and dual-polarization radar measurements in Finland. *J. Geophys. Res. Atmos.*, **124**, 13 273–13 290, https://doi.org/10.1029/2019JD030721.

——, J. Leinonen, D. Moisseev, and T. Nousiainen, 2011: Radar backscattering from snowflakes: Comparison of fractal, aggregate, and soft spheroid models. *J. Atmos. Oceanic Technol.*, **28**, 1365–1372, https://doi.org/10.1175/JTECH-D-11-00004.1.

Vogel, J. M., and F. Fabry, 2018: Contrasting polarimetric observations of stratiform riming and nonriming events. *J. Appl. Meteor. Climatol.*, **57**, 457–476, https://doi.org/10.1175/JAMC-D-16-0370.1.

von Lerber, A., D. Moisseev, L. F. Bliven, W. Petersen, A.-M. Harri, and V. Chandrasekar, 2017: Microphysical properties of snow and their link to Z_e–S relations during BAECC 2014. *J. Appl. Meteor. Climatol.*, **56**, 1561–1582, https://doi.org/10.1175/JAMC-D-16-0379.1.

Wang, P. K., and W. Ji, 2000: Collision efficiencies of ice crystals at low–intermediate Reynolds numbers colliding with supercooled cloud droplets: A numerical study. *J. Atmos. Sci.*, **57**, 1001–1009, https://doi.org/10.1175/1520-0469(2000)057<1001:CEOICA>2.0.CO;2.

Zawadzki, I., F. Fabry, and W. Szyrmer, 2001: Observations of supercooled water and secondary ice generation by a vertically pointing X-band Doppler radar. *Atmos. Res.*, **59-60**, 343–359, https://doi.org/10.1016/S0169-8095(01)00124-7.